

Supporting Information

1
2
3
4
5
6
7
8
9
10
11
12
13
14
15
16
17
18
19
20
21
22
23
24
25
26
27
28
29
30
31
32
33
34

An asymmetric supercapacitor with an interpenetrating crystalline Fe-MOF as positive electrode and its congenetic derivative as negative electrode

Saier Wang ^{a,b}, Shuaishuai Wang^a, Xu Guo^a, Zikai Wang^a, Feifei Mao^a, Lianghu Su^b, Hua Wu,
^{a,*} Kuaibing Wang, ^{a,*} Qichun Zhang ^{c,d,*}

^a Department of Chemistry, College of Sciences
Jiangsu Key Laboratory of Pesticide Sciences
Nanjing Agricultural University
Nanjing 210095, Jiangsu, P. R. China
E-mail: wuhua@njau.edu.cn; wangkb@njau.edu.cn

^b Nanjing Institute of Environmental Sciences, Ministry of Ecology and Environment,
Nanjing 210036, Jiangsu, P. R. China

^c Department of Materials Science and Engineering,
City University of Hong Kong, 83 Tat Chee Avenue
Hong Kong SAR 999077, P. R. China
Email: qiczhang@cityu.edu.hk

^d Center of Super-Diamond and Advanced Films (COSDAF), City University of Hong Kong,
Hong Kong SAR 999077, China

Contents

1

2	1. Experimental section	3
3	1.1 Syntheses of Fe(TATB)(Tipa)(H ₂ O) (FeSC) and Fe ₂ O ₃ /Fe ₃ N/Fe ₃ C (FeSC [#])	3
4	1.2 Materials characterization and methods	3
5	1.3 X-ray Crystallography	4
6	1.4 Electrode preparation	4
7	1.5 Equations	5
8	2. Figures	6
9	Figure S1. (a) 3D framework built from Fe ^{III} and Tipa ligands. (b) 1D chain of -Fe-TATB-Fe.	6
10	Figure S2. TG curve of FeSC.	6
11	Figure S3. EDX mapping spectroscopy of FeSC.....	7
12	Figure S4. EDX mapping spectroscopy of FeSC [#]	7
13	Figure S5. XPS of Fe-MOF and Fe ₂ O ₃ /Fe ₃ N/Fe ₃ C.....	8
14	Figure S6. (a) N 1s XPS of FeSC; (b) C 1s XPS of FeSC; (c) O 1s XPS of FeSC.	8
15	Figure S7. (a) N 1s XPS of FeSC [#] ; (b) C 1s XPS of FeSC [#] ; (c) O 1s XPS of FeSC [#]	8
16	Figure S8. N ₂ adsorption-desorption curves for FeSC a) and FeSC [#] b) samples.	9
17	Figure S9. (a, b) CV curves of FeSC and FeSC [#] , respectively.	9
18	Figure S10. (a, b) Randle–Sevcik plots of FeSC and FeSC [#] , respectively.....	9
19	Figure S11. Equivalent circuit for Fe-based electrodes.	10
20	Figure S12. Schematic diagram of the adsorption/desorption of active site interaction and hydroxide uncoordinated carboxylic O groups and coordinated water molecules.	10
22	Figure S13. (a) CV curves of bare nickel foam, H ₃ TATB, Tipa and FeSC at 30 mV s ⁻¹ ; (b) GCD curves of bare nickel foam, H ₃ TATB, Tipa and FeSC at 1 A g ⁻¹	10
24	Figure S14. Comparison of FeSC powder immersed in 6M KOH for different time	11
25	Figure S15. Potential range of Fe-MOF and Fe ₂ O ₃ /Fe ₃ N/Fe ₃ C in a three-electrode system.	11
26	Figure S16. (a) CV curves of the asymmetric device working at the different potential window; (b) GCD curves of the asymmetric device working at different potential window.	12
28	Figure S17. (a) Specific capacity of asymmetric device at different current densities from 1 to 10 Ag ⁻¹ ; (b) Energy delivery efficiency of asymmetric device.....	12
30	3. Tables	13
31	Table S1. Comparison of electrochemical parameters with other Fe-based electrode materials and pyrolysis of MOF electrode materials.....	13
33	Table S2. Distances [Å] and angles [°] for FeSC.....	14
34	4. References	15
35		

1 **1. Experimental section**

2 **1.1 Syntheses of Fe(TATB)(Tipa)(H₂O) (FeSC) and Fe₂O₃/Fe₃N/Fe₃C (FeSC#)**

3 A mixture of H₃TATB (0.044 g, 0.1 mmol), Fe(SO₄)₂·7H₂O (0.056 g, 0.2 mmol), Tipa
4 (0.022 g, 0.05 mmol), DMF (11 mL) and water (4 mL) was placed in a Teflon reactor (20
5 mL) and heated at 120°C for 3 days. The mixture was cooled to 100 °C at a rate of 10 °C·h⁻¹
6 and then naturally cooled down to room temperature. The resulting crystals were collected
7 and washed with water and methanol, then dried in air for a yield of about 64% based on Fe.
8 The FeSC ground powder was placed in a tube furnace and then heated at 800 °C at a rate of
9 5 °C min⁻¹ and held at flowing N₂ for 2 h. Carbonized black powder of FeSC# was collected
10 and used as an electrode material.

11 **1.2 Materials and methods**

12 All raw materials were commercially purchased from Sinopharm Chemical Reagent, and
13 used as received without further purification. Pro-ligand Tipa was prepared according to the
14 method reported by Wu *et al*¹. The remaining commercially available chemical reagents were
15 of analytical grade and were used without further purification. Surface morphologies were
16 characterized by Hitachi SU8010 field scanning electron microscopy (SEM), FEI Talos 120L
17 Transmission Electron Microscope (TEM) and FEI Tecnai G2 F30 High Resolution
18 Transmission Electron Microscope (HRTEM). FT-IR spectra were recorded in range
19 4000–400 cm⁻¹ from KBr pellets on a Mattson Alpha-Centauri spectrometer. Thirty-two
20 scans were taken of each sample recorded from the range 4000–800 cm⁻¹ at a resolution of
21 2 cm⁻¹ in the transmission mode. A thermogravimetric analysis (TA) experiment was
22 implemented under air atmosphere on a Beijing Hengjiu HTG-1 instrument with a heating
23 rate of 10 °C min⁻¹. Powder X-ray diffraction measurements were performed with a
24 RigakuDmax 2000 X-ray diffractometer with graphite monochromatized. Raman spectra were
25 collected on a HORIBA Scientific LabRAM HR Evolution Raman spectrophotometer with

1 514 nm laser radiation in the range of 100–2000 cm^{-1} . Surface element composition and
2 valence of the sample were measured by a Thermo Kalpha X-ray photoelectron spectroscopy.
3 N_2 isotherms were measured using a Micromeritics ASAP 2460 analyzer at $-198\text{ }^\circ\text{C}$.

4

5 **1.3 X-ray Crystallography**

6 Single-crystal X-ray diffraction data for **FeSC** and was collected with a Bruker Smart CCD
7 Diffraction at room temperature, using a ω scan technique Mo-K α radiation ($\lambda = 0.71073\text{ \AA}$).
8 Crystal data for compound **FeSC**: monoclinic, $a = 24.932(3)\text{ \AA}$, $b = 15.8670(16)\text{ \AA}$, $c =$
9 $22.885(3)\text{ \AA}$, $\alpha = 90^\circ$, $\beta = 90.394(11)^\circ$, $\gamma = 90^\circ$, $V = 9053.0(17)\text{ \AA}^3$, space group $C2/c$, $Z = 8$,
10 33071 reflections measured, 11071 unique reflections ($R_{\text{int}} = 0.0369$). The final R_1 and $wR(F_2)$
11 values for $I > 2\sigma(I)$ were 0.0472 and 0.1320, then for all data values were 0.0766 and 0.1537,
12 respectively. The goodness of fit on F^2 was 1.025. The CCDC number is 2044228. Selected
13 distances [\AA] and angles [$^\circ$] for FeSC are listed in Table S2.

14

15 **1.4 Electrode preparation**

16 Working electrode preparation for the traditional three-electrode system: 75 mg of the
17 active sample and 15 mg of acetylene black were ground for 20 minutes, and then 10 g
18 adhesive PTEF 10 mg was added. The mixed sample was dissolved in isopropanol and stirred
19 for 24 hours, and the as-obtained slurry was applied on the surface of the foamed nickel with
20 a region of $1 \times 1\text{ cm}^2$ and a mass load of $2\text{--}4\text{ mg cm}^{-2}$. The coated nickel foam was dried at 75
21 degrees for 2 hours and pressed into a thin foil under a pressure of approximately 10.0 MPa to
22 obtain a working electrode. A three-electrode system was constructed with platinum wire used
23 as the counter electrode, saturated calomel as the reference electrode, and 6M KOH as the
24 electrolyte.

25 Manufacture of aqueous asymmetric supercapacitor device: FeSC and FeSC[#] were used
26 as positive and negative electrodes, respectively. The masses of the positive and negative

1 materials are 2.0 mg and 6.6 mg, which is consistent with the mass ratio of 1:3.3 calculated
2 according to the specific capacitance. The electrochemical performance of the two-electrode
3 electrochemical full cell was measured at room temperature with 6M KOH as the electrolyte.

4

5 1.5 Equations

6 The material mass ratio of the positive and negative electrodes of the device is calculated
7 according to equation:

$$8 \quad \frac{m^+}{m^-} = \frac{C_m^+ \times \Delta V^+}{C_m^- \times \Delta V^-} \quad (1)$$

9 Specific capacitances derived from galvanostatic charge-discharge (GCD) tests can be
10 determined from the equation:

$$11 \quad C_s = \frac{I \times \Delta t}{m \times \Delta V} \quad (2)$$

12 Where C_s refers to the specific capacitance ($F g^{-1}$), I represents current density ($A g^{-1}$), Δt
13 denotes the discharge time (s), m corresponds to the mass of active material (g), ΔV shows
14 voltage window (V).

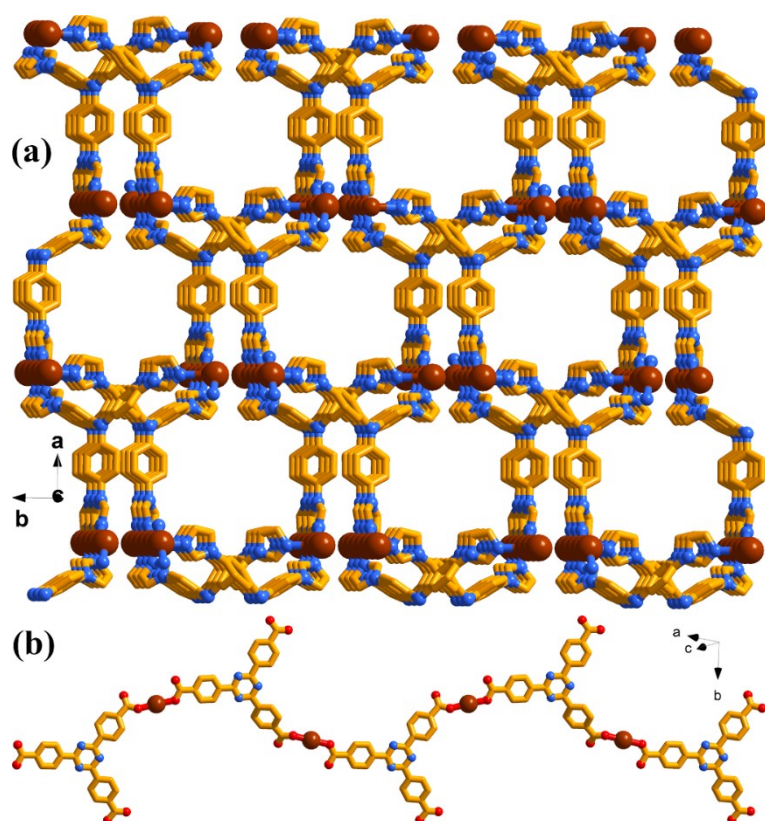
15 Energy density (E_s) and power density (P_s) of the supercapacitor device can be
16 calculated from :

$$17 \quad E_s = \frac{C_{cell} \times \Delta V^2}{2 \times 3.6} \quad (3)$$

$$18 \quad P_s = 3600 \times \frac{E_s}{\Delta t} \quad (4)$$

19 Where C_{cell} refers to the specific capacitance ($F g^{-1}$), ΔV represents the operating voltage
20 (V), Δt denotes the discharge time (s).

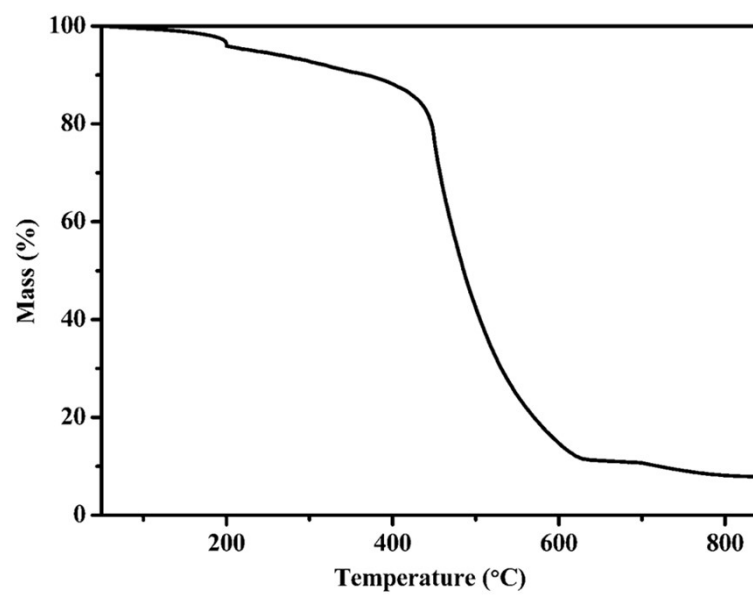
21 2. Figures



1

2 **Figure S1.** (a) 3D framework built from Fe^{III} and Tipa ligands. (b) 1D chain of -Fe-TATB-Fe.

3



4

5

6

7

Figure S2. TG curve of FeSC.

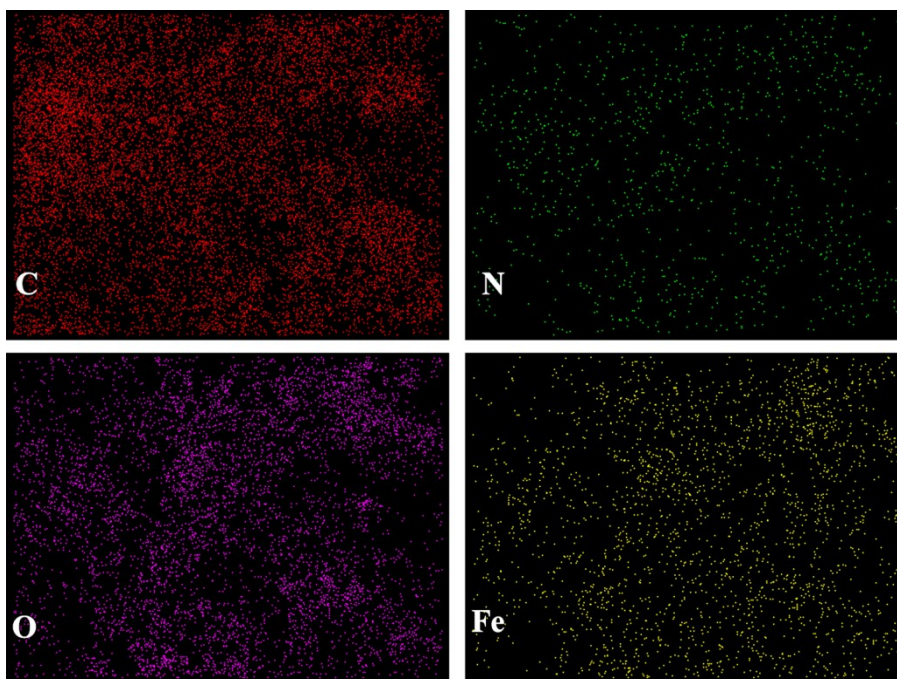


Figure S3. EDX mapping spectroscopy of FeSC.

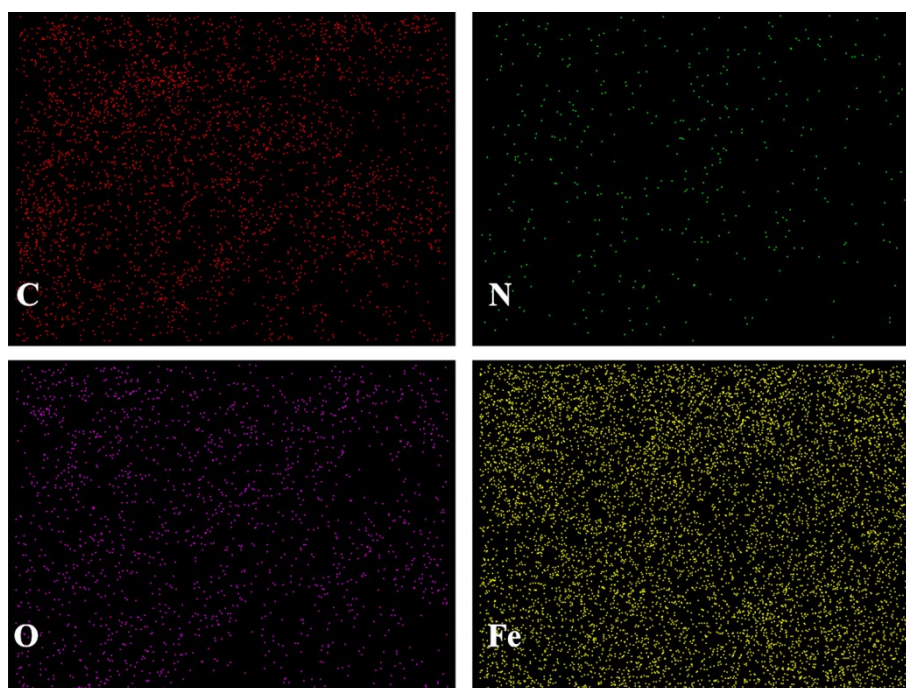
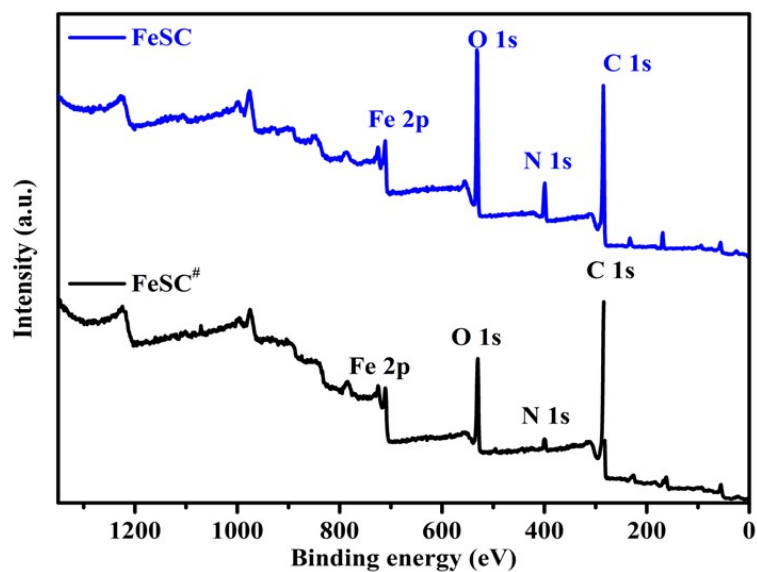


Figure S4. EDX mapping spectroscopy of FeSC#.

1
2
3

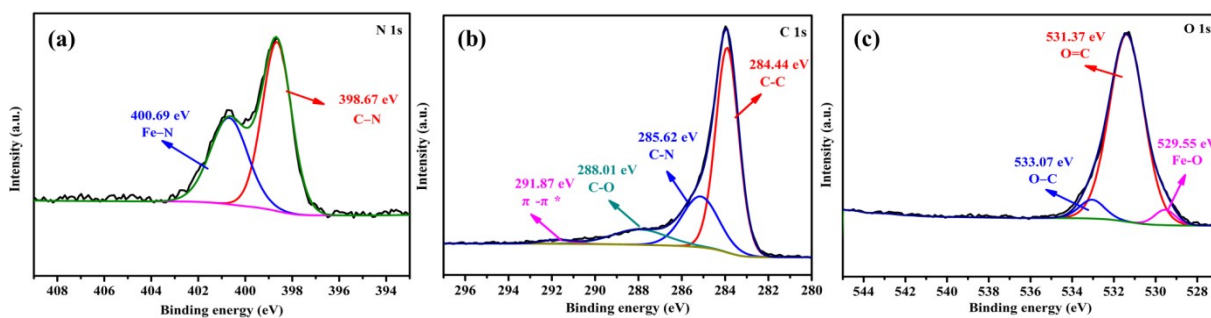
4
5
6
7
8



1

2 **Figure S5.** XPS of Fe-MOF and Fe₂O₃/Fe₃N/Fe₃C.

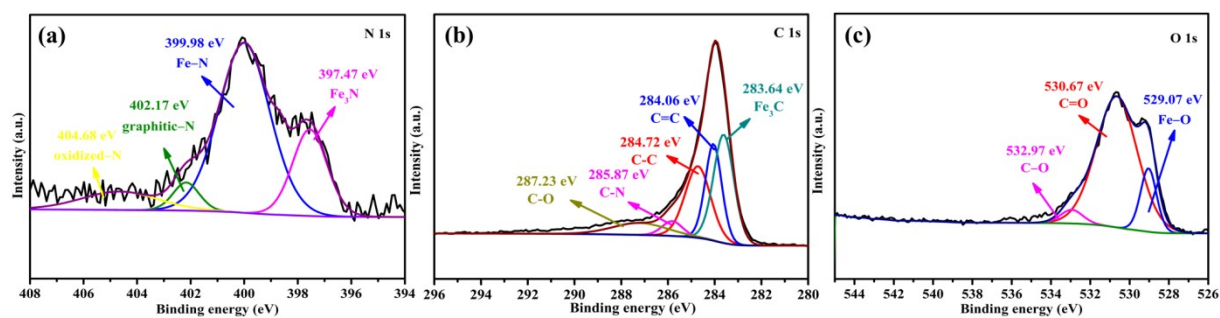
3



4

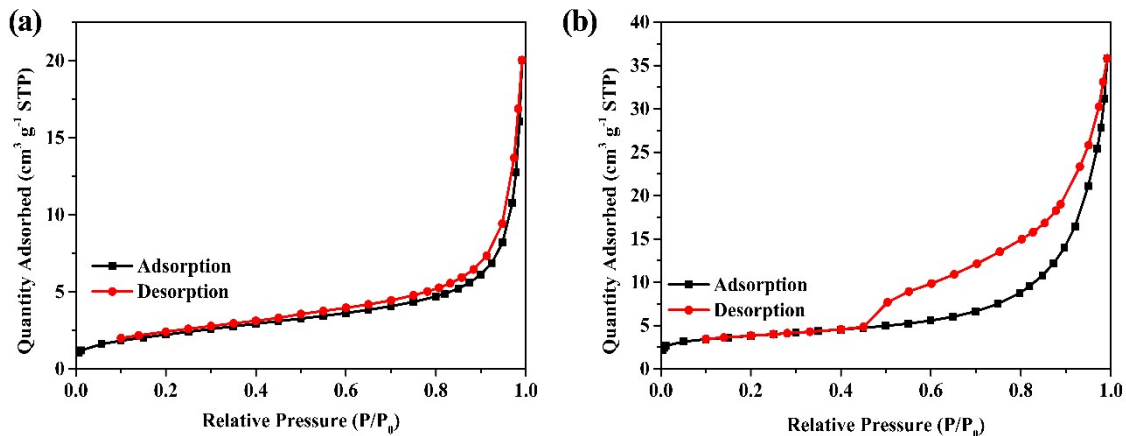
5 **Figure S6.** (a) N 1s XPS of FeSC; (b) C 1s XPS of FeSC; (c) O 1s XPS of FeSC.

6



7

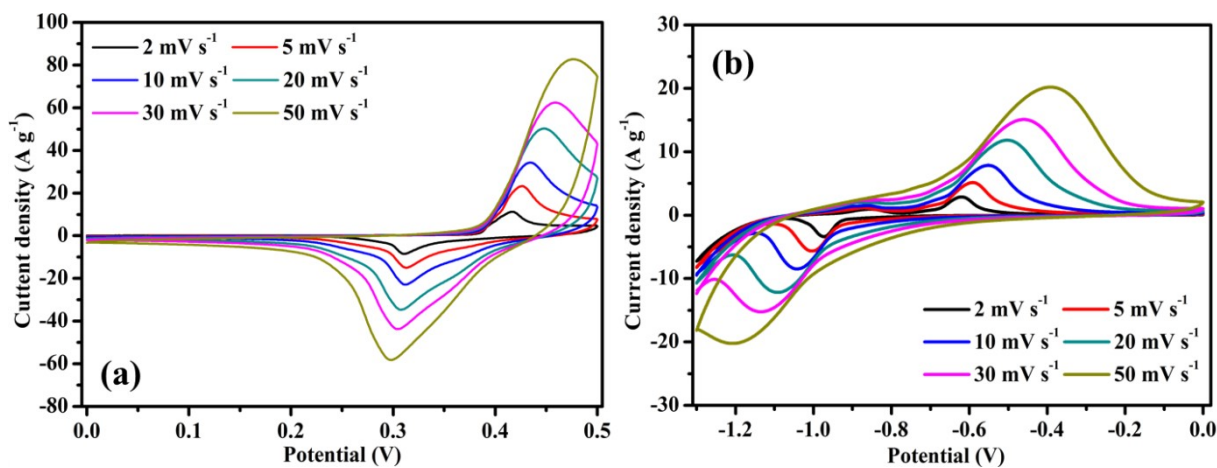
8 **Figure S7.** (a) N 1s XPS of FeSC[#]; (b) C 1s XPS of FeSC[#]; (c) O 1s XPS of FeSC[#].



1

2 **Figure S8.** N₂ adsorption-desorption curves for FeSC a) and FeSC[#] b) samples.

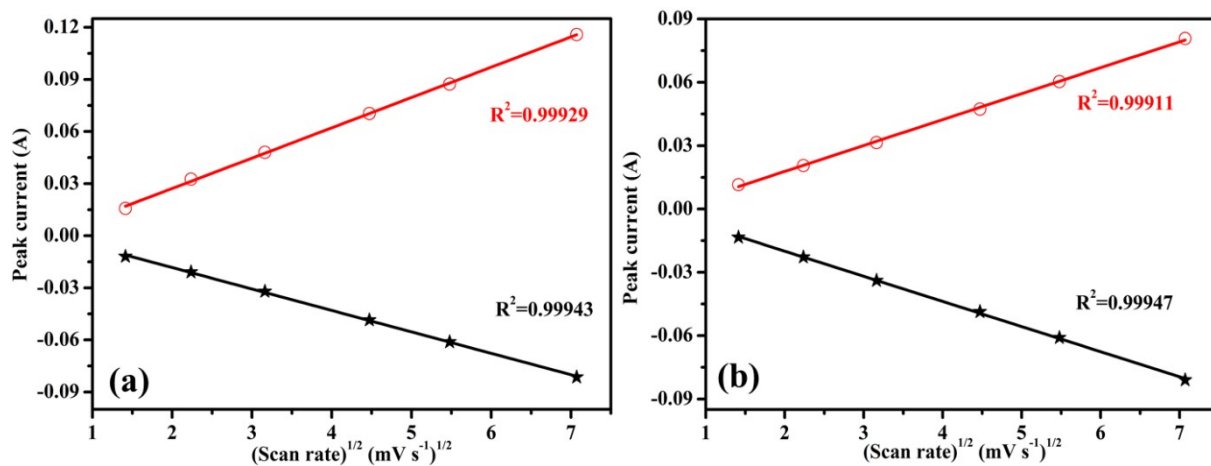
3



4

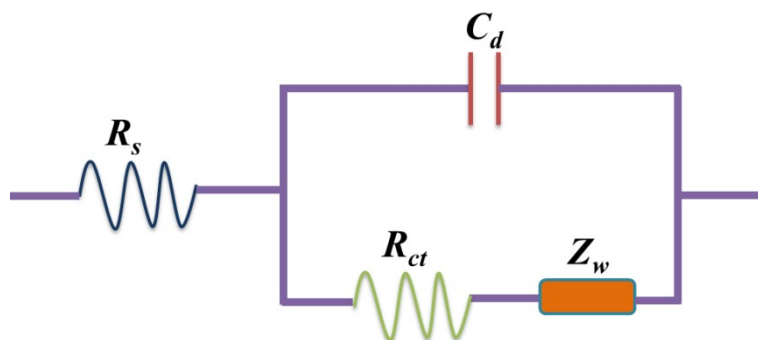
5 **Figure S9.** (a, b) CV curves of FeSC and FeSC[#], respectively.

6



7

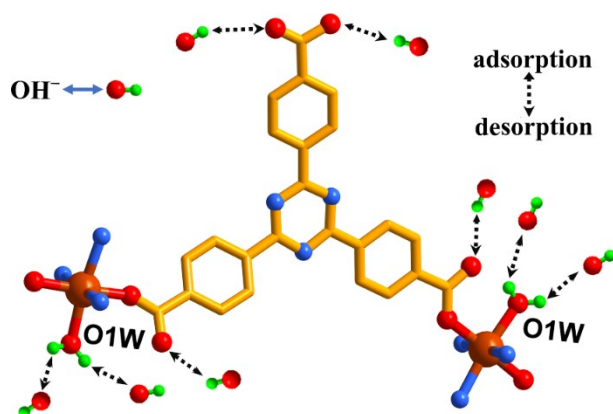
8 **Figure S10.** (a, b) Randle-Sevcik plots of FeSC and FeSC[#], respectively.



1

2 **Figure S11.** Equivalent circuit for Fe-based electrodes.

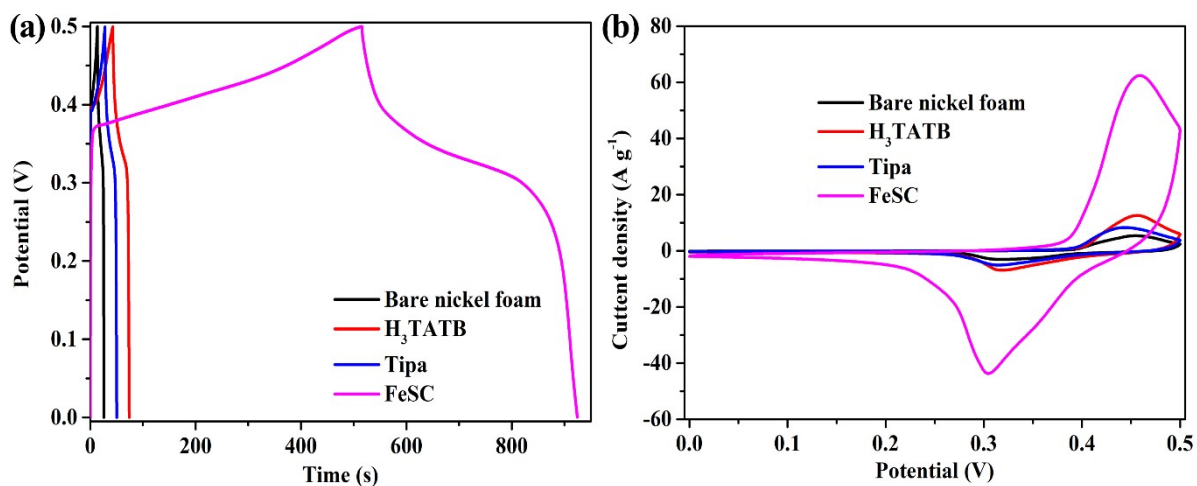
3



4

5 **Figure S12.** Schematic diagram of the adsorption/desorption of active site interaction and hydroxide
6 uncoordinated carboxylic O groups and coordinated water molecules.

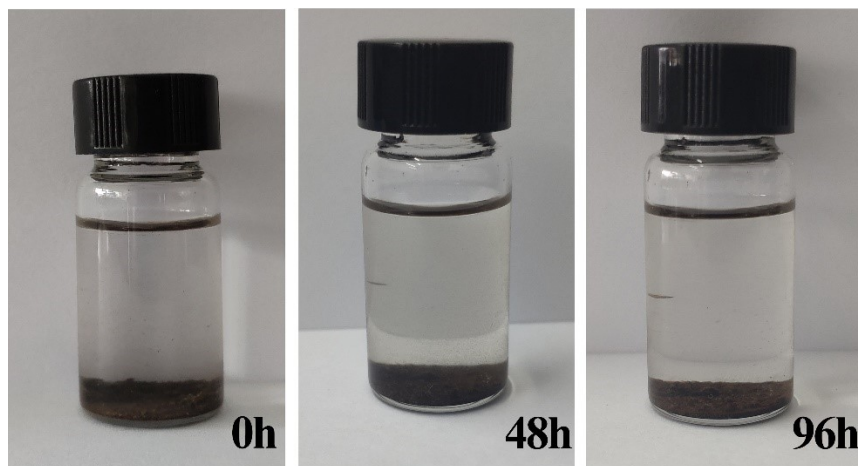
7



8

9 **Figure S13.** (a) CV curves of bare nickel foam, H₃TATB, Tipa and FeSC at 30 mV s⁻¹; (b) GCD curves of
10 bare nickel foam, H₃TATB, Tipa and FeSC at 1 A g⁻¹.

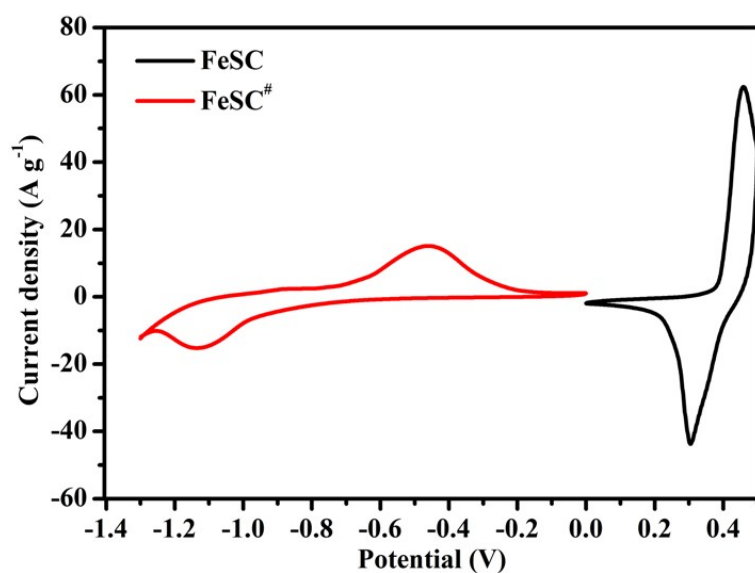
11



1

2 **Figure S14.** Comparison of FeSC powder immersed in 6M KOH for different time

3



4

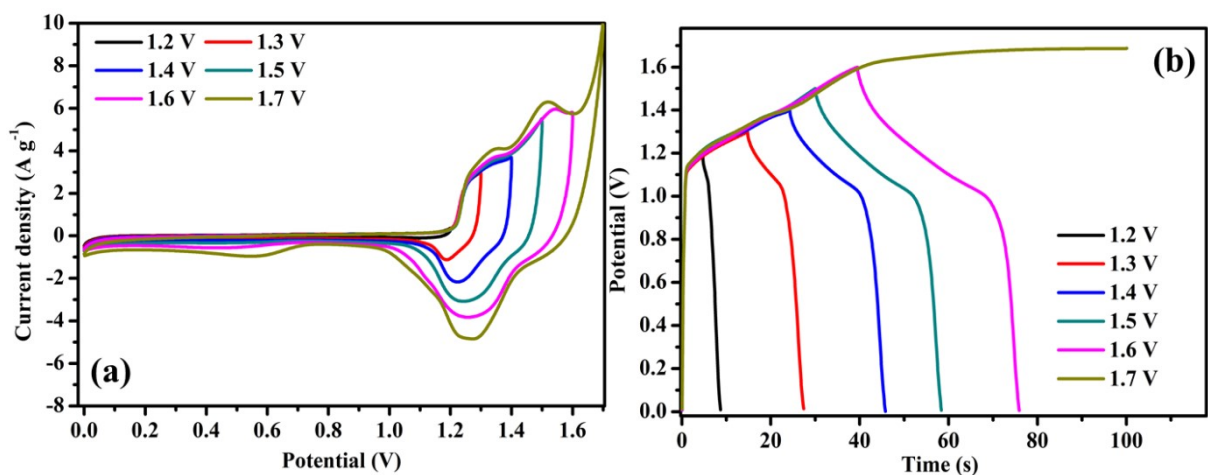
5 **Figure S15.** Potential range of Fe-MOF and Fe₂O₃/Fe₃N/Fe₃C in a three-electrode system.

6

7

8

9

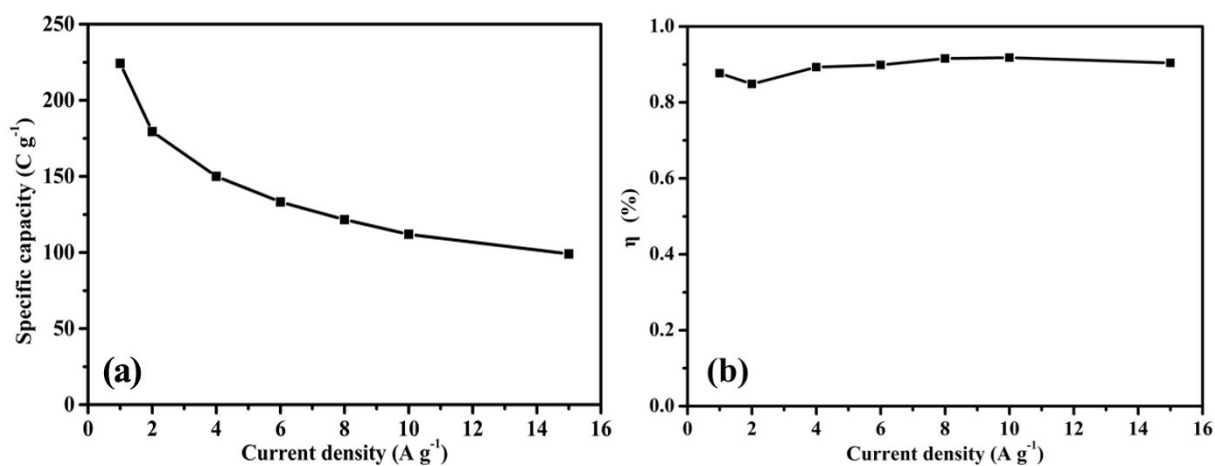


1

2 **Figure S16.** (a) CV curves of the asymmetric device working at the different potential window; (b) GCD

3 curves of the asymmetric device working at different potential window.

4



5

6 **Figure S17.** (a) Specific capacity of asymmetric device at different current densities from 1 to 10 A g^{-1} ; (b)

7 Energy delivery efficiency of asymmetric device.

8

9

10

11

12

13

14

15

16

1 3. Tables

2 **Table S1** Comparison of electrochemical parameters with other Fe-based electrode materials and pyrolysis
3 of MOF electrode materials.

Electrode	Electrolyte	Potential (V)	Capacitance@CD ^a
FeSC (This work)	6 M KOH	0 ~ 0.5	824.6 F g ⁻¹ @ 1 A g ⁻¹
FeSC [#] (This work)	6 M KOH	-1 ~ 0	377 F g ⁻¹ @ 1 A g ⁻¹
Fe-MnO ₂ ²	1 M Na ₂ SO ₄	0 ~ 1	350 F g ⁻¹ @ 1 A g ⁻¹
Fe/Fe ₃ O ₄ @CNTs/CNFs ³	1 M KOH	-1 ~ 0	195 F g ⁻¹ @ 0.5 A g ⁻¹
Mn ₃ O ₄ -Fe ₃ O ₄ @C ⁴	1 M NaCl	-0.45 ~ 1.2	178 F g ⁻¹ @ 1 A g ⁻¹
Fe ₃ O ₄ @N-doped carbon ⁵	6 M KOH	-1.0 ~ 0	206 F g ⁻¹ @ 1 A g ⁻¹
LaFeO ₃ NFs ⁶	6 M KOH	0 ~ 0.5	183.6 F g ⁻¹ @ 1 A g ⁻¹
Fe(PO ₃) ₃ ⁷	3 M KOH	0 ~ 0.5	392.5 F g ⁻¹ @ 1 A g ⁻¹
Fe(III)/BiOCl ⁸	1 M H ₂ SO ₄	0 ~ 0.5	540 F g ⁻¹ @ 1 A g ⁻¹
Fe ₂ O ₃ /RGO/Fe ₃ O ₄ ⁹	2 M KOH	-1.2 ~ 0.4	337.5 mF cm ⁻² @ 20 mA cm ⁻²
Ni-Co-Fe fluorides ¹⁰	6 M KOH	0 ~ 0.5	738.0 F g ⁻¹ @ 1 A g ⁻¹
pyrolysis of MIL-101 (Fe _x O _y /C) ¹¹	6 M KOH	-1 ~ 0	114 F g ⁻¹ @ 2 A g ⁻¹
pyrolysis of Fe-MOF gel (Fe ₃ C/C) ¹²	6 M KOH	-1.1 ~ 0	184 mAh g ⁻¹ @ 1 A g ⁻¹
pyrolysis of MIL-47 (porous carbon) ¹³	6 M KOH	-1 ~ 0	326 F g ⁻¹ @ 0.5 A g ⁻¹
pyrolysis of Zn-MOF (nanoporous carbon) ¹⁴	1 M H ₂ SO ₄	-0.2 ~ 0.8	477.7 F g ⁻¹ @ 0.2 A g ⁻¹
pyrolysis of ZIF-67 (Co ₃ O ₄ /WO ₃) ¹⁵	1 M H ₂ SO ₄	0 ~ 1	553 F g ⁻¹ @ 1 A g ⁻¹
pyrolysis of Cu@Co-MOF ¹⁶	2 M KOH	0 ~ 0.5	563.8 F g ⁻¹ @ 1 A g ⁻¹
pyrolysis of Ni-MOF/GO ¹⁷	6 M KOH	0 ~ 0.5	992 F g ⁻¹ @ 1 A g ⁻¹
pyrolysis of Cu-BTC ¹⁸	3 M KOH	0 ~ 0.5	729 F g ⁻¹ @ 1 A g ⁻¹

4 ^aCD means current density.

5

6

7

1 **Table S2.** Distances [Å] and angles [°] for FeSC.

Fe(1)-O(6) ^{#1}	2.0372(16)	Fe(1)-N(4)	2.153(2)
Fe(1)-O(1)	2.0653(14)	Fe(1)-O(1W)	2.1840(18)
Fe(1)-N(10) ^{#2}	2.1364(19)	Fe(1)-N(8) ^{#3}	2.211(2)
O(6) ^{#1} -Fe(1)-O(1)	177.34(7)	N(4)-Fe(1)-O(1W)	93.23(8)
O(6) ^{#1} -Fe(1)-N(10) ^{#2}	88.92(8)	O(6) ^{#1} -Fe(1)-N(8) ^{#3}	84.27(8)
O(1)-Fe(1)-N(10) ^{#2}	88.78(7)	O(1)-Fe(1)-N(8) ^{#3}	94.50(7)
O(6) ^{#1} -Fe(1)-N(4)	94.97(8)	N(10) ^{#2} -Fe(1)-N(8) ^{#3}	93.06(8)
O(1)-Fe(1)-N(4)	87.27(7)	N(4)-Fe(1)-N(8) ^{#3}	85.19(8)
N(10) ^{#2} -Fe(1)-N(4)	175.55(8)	O(1W)-Fe(1)-N(8) ^{#3}	173.48(7)
O(6) ^{#1} -Fe(1)-O(1W)	89.57(7)	N(10) ^{#2} -Fe(1)-O(1W)	88.94(8)
O(1)-Fe(1)-O(1W)	91.75(7)		

2 Symmetry transformations used to generate equivalent atoms: ^{#1} x+1/2, -y+1/2, z+1/2, ^{#2} x-1/2, -y+1/2,

3 z+1/2, ^{#3} x-1/2, y+1/2, z.

1 References

- 2 1. K. Wang, X. Wang, D. Zhang, H. Wang, Z. Wang, M. Zhao, R. Xi, H. Wu and M.
3 Zheng, Interpenetrated nano-MOFs for ultrahigh-performance supercapacitors and
4 excellent dye adsorption performance, *CrystEngComm*, 2018, **20**, 6940-6949.
- 5 2. N. Zarshad, J. Wu, A. U. Rahman and H. Ni, Fe-MnO₂ core-shell heterostructure for
6 high-performance aqueous asymmetrical supercapacitor, *J. Electroanal. Chem.*, 2020,
7 **871**, 114266.
- 8 3. F. Aftab, S. Tanveer, S. U. Rehman, S. Ghafoor, H. Duran, K. Kirchhoff, I.
9 Lieberwirth and S. N. Arshad, Encapsulation of Fe/Fe₃O₄ in carbon nanotubes grown
10 over carbon nanofibers for high performance supercapacitor electrodes, *Synthetic Met.*,
11 2020, **269**, 116575.
- 12 4. B. Hu, Y. Wang, X. Shang, K. Xu, J. Yang, M. Huang and J. Liu, Structure-tunable
13 Mn₃O₄-Fe₃O₄@C hybrids for high-performance supercapacitor, *J. Colloid Interface*
14 *Sci.*, 2021, **581**, 66-75.
- 15 5. X. Zhu, D. Hou, H. Tao and M. Li, Simply synthesized N-doped carbon supporting
16 Fe₃O₄ nanocomposite for high performance supercapacitor, *J. Alloys Compd.*, 2020,
17 **821**, 153580.
- 18 6. Q. Hu, B. Yue, H. Shao, F. Yang, J. Wang, Y. Wang and J. Liu, Facile syntheses of
19 perovskite type LaMO₃ (M=Fe, Co, Ni) nanofibers for high performance
20 supercapacitor electrodes and lithium-ion battery anodes, *J. Alloys Compd.*, 2021, **852**,
21 157002.
- 22 7. B. Li, H. Pang and H. Xue, Fe-based phosphate nanostructures for supercapacitors,
23 *Chin. Chem. Lett.*, 2020, DOI: 10.1016/j.ccllet.2020.07.004.
- 24 8. R. Rameshbabu, M. Sandhiya and M. Sathish, Fe(III) ions grafted bismuth
25 oxychloride nanosheets for enhanced electrochemical supercapacitor application, *J.*
26 *Electroanal. Chem.*, 2020, **862**, 113958.

- 1 9. C. Zhao, X. Shao, Y. Zhang and X. Qian, Fe₂O₃/Reduced Graphene Oxide/Fe₃O₄
2 Composite in Situ Grown on Fe Foil for High-Performance Supercapacitors, *ACS Appl.*
3 *Mater. Interfaces*, 2016, **8**, 30133-30142.
- 4 10. X. Zhou, H. Dai, X. Huang, Y. Ren, Q. Wang, W. Wang, W. Huang and X. Dong,
5 Porous trimetallic fluoride Ni–Co–M (M = Mn, Fe, Cu, Zn) nanoprisms as electrodes
6 for asymmetric supercapacitors, *Mater. Today Energy*, 2020, **17**, 100429.
- 7 11. A. Farisabadi, M. Moradi, S. Hajati, M. A. Kiani and J. P. Espinos, Controlled
8 thermolysis of MIL-101(Fe, Cr) for synthesis of Fe_xO_y/porous carbon as negative
9 electrode and Cr₂O₃/porous carbon as positive electrode of supercapacitor, *Appl. Surf.*
10 *Sci.*, 2019, **469**, 192-203.
- 11 12. Y. Zhang, R. Shao, W. Xu, J. Ding, Y. Wang, X. Yan, W. Shi and M. Wang, Soluble
12 salt assisted synthesis of hierarchical porous carbon-encapsulated Fe₃C based on
13 MOFs gel for all-solid-state hybrid supercapacitor, *Chem. Eng. J.*, 2021, **419**, 129576.
- 14 13. H. Li, J. Wu, L. Wang, Q. Liao, X. Niu, D. Zhang and K. Wang, A zinc ion hybrid
15 capacitor based on sharpened pencil-like hierarchically porous carbon derived from
16 metal–organic framework, *Chem. Eng. J.* 2022, **428**, 131071.
- 17 14. M. Yao, X. Zhao, Q. Zhang, Y. Zhang and Y. Wang, Polyaniline nanowires aligned on
18 MOFs-derived nanoporous carbon as high-performance electrodes for supercapacitor,
19 *Electrochim. Acta*, 2021, **390**, 138804.
- 20 15. S. Sundriyal, V. Shrivastav, A. Gupta, V. Shrivastav, A. Deep and S. R. Dhakate,
21 Pencil peel derived mixed phase activated carbon and metal-organic framework
22 derived cobalt-tungsten oxide for high-performance hybrid supercapacitors, *Mater.*
23 *Res. Bull.*, 2021, **142**, 111396.
- 24 16. R. Yuan, H. Li, X. Yin, P. Wang, J. Lu and L. Zhang, Construction of multi-structures
25 based on Cu NWs-supported MOF-derived Co oxides for asymmetric
26 pseudocapacitors, *J. Mater. Sci. & Technol.*, 2021, **65**, 182-189.

- 1 17. Z. Zhang, H. Huo, J. Gao, Z. Yu, F. Ran, L. Guo, S. Lou, T. Mu, X. Yin, Q. Wang and
2 G. Yin, Ni-MOF derived NiO/C nanospheres grown in situ on reduced graphene oxide
3 towards high performance hybrid supercapacitor, *J. Alloy. Compd.*, 2019, **801**, 158-
4 165.
- 5 18. D. Khalafallah, J. Miao, M. Zhi and Z. Hong, Structuring graphene quantum dots
6 anchored CuO for high-performance hybrid supercapacitors, *J. Taiwan Inst. Chem. E.*,
7 2021, **122**, 168-175.
- 8